Article

Elucidating the Role of the Metal Catalyst and Oxide Support in the Ru/CeO₂-Catalyzed CO₂ Methanation Mechanism

Sergio López-Rodríguez, Arantxa Davó-Quiñonero,* Esther Bailón-García, Dolores Lozano-Castelló, Facundo C. Herrera, Eric Pellegrin, Carlos Escudero, Max García-Melchor,* and Agustín Bueno-López*

Read Online

ACCESS | Metrics & More | Article Recommendations | Supporting Information

ABSTRACT: This study addresses the yet unresolved CO_2 methanation mechanism on a Ru/CeO₂ catalyst by means of near-ambient-pressure X-ray photoelectron spectroscopy (NAP−XPS) and diffuse reflectance infrared Fourier transform spectroscopy (DRIFTS) complemented with periodic density functional theory (DFT) calculations. NAP−XPS results show that the switch from H_2 to $CO_2 + H_2$ mixture oxidizes both the Ru and CeO₂ phases at low temperatures, which is explained by the CO_2 adsorption modes assessed by means of DFT on each representative surface. CO_2 adsorption on Ru is dissociative and moderately endergonic, leading to polybonded Ru-carbonyl groups whose hydrogenation is the rate-determining step in the overall

process. Unlike on Ru metal, CO_2 can be strongly adsorbed as carbonates on ceria surface oxygen sites or on the reduced ceria at oxygen vacancies as carboxylates ($CO_2^{-\delta}$), resulting in the reoxidation of ceria. Carboxylates can then evolve as CO, which is released either via direct splitting at relatively low temperatures or through stable formate species at higher temperatures. DRIFTS confirm the great stability of formates, whose depletion relates with CO_2 conversion in the reaction cell, while carbonates remain on the surface up to higher temperatures. CO generation on ceria serves as an additional reservoir of Ru-carbonyls, cooperating to the overall CO_2 methanation process. Altogether, this study highlights the noninnocent role of the ceria support in the performance of Ru/CeO₂ toward CO_2 methanation.
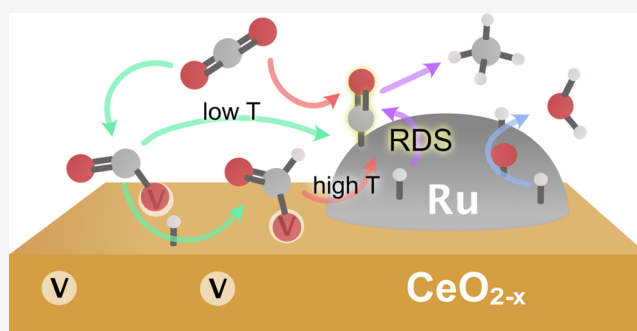
1. INTRODUCTION

The global warming induced by the rising energy-related CO_2 emissions is a threat that has become a primary focus for environmental research. Moreover, according to official forecasts, the energy demand will grow by 33% in 2050 compared to 2017 together with the CO_2 emissions over the next years.[1] Hence, supplying this demand while meeting the CO_2 emission targets is a major challenge that society has to face in the 21st century via the implementation of sustainable policies and energy practices with a lower carbon footprint.[2] In this scenario, scientists and industrial stakeholders are urged to design alternative technologies to enable a feasible and successful transition from carbon-based to renewable fuels. This involves the deployment of new hydrogen power plants and the reduction of carbon dioxide emissions according to the established pillars of the circular economy.[3,4] In this regard, the CO_2 methanation reaction is an attractive strategy.[5,6] This process consists in the conversion of CO_2 to CH_4, a valuable fuel so-called synthetic natural gas, using hydrogen as shown in eq 1

$$CO_2 + 4H_2 \rightarrow CH_4 + 2H_2O, \quad \Delta H^0 = -164 \text{ kJ mol}^{-1}$$

(1)
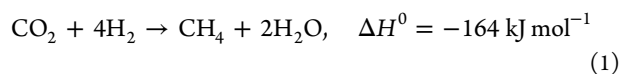
As a remarkable positive incentive, CO_2 methanation technologies based on captured CO_2 and green hydrogen[7] can enable a clean energy distribution without the requirement of new infrastructure or alternative combustion engines.[8] Furthermore, CO_2 methanation can be deemed carbon-neutral if both hydrogen and the thermal activation energy required are supplied from renewable sources and the CO_2 released upon the eventual CH_4 utilization is captured and fed back into the methanation process.

In general terms, CO_2 methanation is spontaneous at ambient temperature, but the use of active catalysts is needed to overcome the sluggish reaction kinetics to reach relevant reaction rates and selectivities for industrial applications.[9] Among the studied active phases, nickel is a well-known cost-effective CO_2 methanation catalyst that operates between 300 and 450 °C providing good CH_4 selectivity. When finely
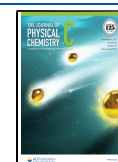
dispersed as Ni nanoparticles, the choice of the support determines the overall performance. For example, literature reports have shown that CO_2 Ni/CeO_2 formulations are more active than their counterparts with TiO_2, Al_2O_3, and ZrO_2.[10−17] Such improved performance is generally attributed to the well-known oxygen storage capacity and oxygen mobility in ceria.[10,18−21] Yet, Ni catalysts suffer from sintering and the reverse water gas-shift reaction (RWGS) at high operating temperatures, which compromises CH_4 selectivity and CO_2 conversion.

On the other hand, noble-metal-based catalysts such as Rh, Pt, Pd, and Ru[22−27] exhibit a lower CO_2 methanation onset than Ni (from *ca.* 250 °C to *ca.* 180 °C) enabling us to operate at temperatures where the RWGS is rendered thermodynamically unfavorable. Among precious metals, Ru has received great attention[28−36] and the CO_2 methanation mechanism on this metal catalyst has been investigated in detail.[30,36,37] However, many important aspects of the underlying mechanism still remain unclear and no general consensus has been reached yet, mainly due to the strong structure-sensitive nature of this reaction.[24,38,39] On the one hand, many studies have reported plausible reaction pathways featuring formates (*OCHO, where * denotes a surface-active site) as key intermediates formed upon CO_2 adsorption on H-terminated Ru surfaces. According to this approach, further hydrogenation steps from formates using chemisorbed *H would give rise to *C_xH_yO intermediate species up to methane.[19,22,35,40,41] On the other hand, alternative mechanisms for the Ru-catalyzed methanation have been proposed by different authors. Proaño et al.[41] postulated that Ru-carbonyls are direct precursors of CH_4 on Ru/TiO_2 catalysts. On the contrary, Falbo et al.[30] proposed a mechanism for Ru/Al_2O_3, wherein CO_2 is adsorbed as a bicarbonate on the support and subsequently hydrogenated to CH_4 on Ru, involving formate and carbonyl intermediates. For Ru/CeO_2, Wang et al.[42,43] reported that CO_2 methanation involves formate intermediates, which dissociate on the vacancy sites in ceria. Despite all of these insights, the detailed roles of ruthenium, the ceria support, and the interfacial sites remain unclear. Similarly to Ni, CeO_2 and CeO_2-modified supports provide enhanced activity for Ru catalysts,[29,44,45] although the nature of their active sites is not completely understood either.

Herein, we report a thorough mechanistic investigation of the CO_2 methanation reaction on a high-performance Ru/CeO_2 catalyst using advanced spectroscopy techniques and periodic density functional theory (DFT) calculations. The changes in the electronic structure of Ru and Ce were monitored under reaction conditions using synchrotron radiation by *in situ* near-ambient-pressure X-ray photoelectron spectroscopy (NAP−XPS). DFT calculations, together with *in situ* diffuse reflectance infrared Fourier transform (DRIFT) spectroscopy experiments, were used to identify the active sites and the role of the chemisorbed species during reaction. Altogether, this multidisciplinary study demonstrates that CO_2 is activated on ruthenium, leading to strongly bound carbonyl species, while the main role of ceria is to promote CO_2 chemisorption in the form of carbonates and carboxylates. Further activation of CO_2 on ceria is found to proceed via the decomposition of formate species on surface oxygen vacancies in complementary action to ruthenium. DFT calculations also indicate that the hydrogenation of Ru-carbonyls is the rate-determining step (RDS), while the subsequent hydrogenation of CO_xH intermediates is thermodynamically driven.

2. MATERIALS AND METHODS

2.1. Catalyst Synthesis and Characterization. Cerium oxide support was obtained by calcination of $Ce(NO_3)_3 \cdot 6H_2O$ (99.0%, Sigma-Aldrich) for 6 h at 600 °C. Ruthenium was loaded by incipient wetness impregnation of ruthenium(III) acetylacetonate (97.0%, Sigma-Aldrich) dissolved in toluene to achieve a nominal 4% w. Finally, to obtain the Ru/CeO_2 catalyst, the impregnated sample was heated under N_2 atmosphere at a 5 °C/min pace up to 350 °C and was kept at this temperature for 3 h. General characterization results are presented in the Supporting Information, including N_2 adsorption−desorption isotherms (Table S1, Figure S1), X-ray diffraction (Figure S2), and temperature-programmed reduction with H_2 (Figure S3).

2.2. CO_2 Methanation Catalytic Tests. CO_2 methanation activity tests were performed in a fixed-bed tubular reactor (10 mm inner diameter) containing 200 mg of catalyst mixed with SiC particles (1.00−1.25 mm) to reach the bed volume of 1 cm^3. The catalyst was pretreated *in situ* at 550 °C for 1 h under 200 mL/min of a 50% H_2/N_2 mixture. Once this pretreatment was completed, and after cooling down to 100 °C, the reaction mixture was introduced into the reactor. The feed consisted of 200 mL/min of 16% CO_2, 64% H_2, and 20% N_2 at atmospheric pressure. The GHSV was 9000 h^{-1}, and the temperature was increased in steps of 100 °C up to 325 °C. The gas composition was monitored under steady-state conditions at each temperature with specific gas analyzers (AwiteFLEX COOL; NDIR, electrochemical and thermal conductivity detectors) for CO, CO_2, CH_4, O_2, and H_2. A cold trap at −96 °C is placed after the reactor to condense the released water vapor prior to the detectors. The measured outlet concentrations are rescaled to keep the mol balance.

2.3. *In Situ* NAP−XPS Experiments. X-ray photoemission spectra were recorded *in situ* under methanation conditions at the near-ambient-pressure photoemission (NAPP) branch from CIRCE beamline at the ALBA Synchrotron Light Source facility,[46] which allows tuning the photon energy within 100−2000 eV using a PHOIBOS NAP150 energy analyzer (SPECS GmbH). In each experiment, samples were exposed in the analysis chamber to the reaction mixture consisting of 16% CO_2, 64% H_2, and 20% N_2. Two photon energies were used for each region of interest to obtain information at different surface depths, namely, 1372 and 1082 eV for the Ce 3d region, and 972 and 722 eV for the Ru 3d region. The inelastic mean free path for the emitted photoelectrons through the different pure solid phases of Ru and Ce at each energy utilized during the experiments is presented in Table S3.[47]

The Ru/CeO_2 sample was pelletized and mounted on a gold mesh to minimize charging during the measurements and to provide an energy reference (Au $4f_{7/2}$ peak at 84.0 eV). An infrared laser system (808 nm) was used to heat the samples while the temperature was monitored using a K-type thermocouple. The pressure in the analysis chamber was kept at 1 mbar during the reaction. The catalyst was pretreated *in situ* at 550 °C for 1 h with 50% H_2/N_2 and then cooled down to 100 °C. After this procedure, the methanation mixture was fed at 30 mL/min and the temperature was increased in steps of 50 °C until 450 °C. The reaction was monitored with a mass spectrometer (MKS Instruments) installed at the second stage of the differential pumping system of the analyzer, and XPS measurements were recorded at each temperature under steady-state conditions.

2.4. *In Situ* DRIFTS Experiments. *In situ* DRIFTS experiments were performed in a Jasco infrared spectrometer, model FT/IR-4000, a Praying Mantis high-temperature reaction chamber (Harrick Scientific) with temperature and gas flow control. DRIFT spectra were recorded using a thermoelectrically liquid nitrogen-cooled photoconductive HgCdTe (mercury cadmium telluride, MCT) detector. The gas composition was monitored during the experiments with a Pfeiffer Vacuum mass spectrometer (OmniStar). The catalytic bed consisted of 90 mg of catalyst, which was pretreated in 50% H_2/He at 450 °C for 1 h and then cooled down to room temperature under He atmosphere. A background spectrum was recorded under these conditions, and then the methanation mixture (10% CO_2, 40% H_2 in He balance) was fed at 100 mL/min. Spectra were recorded from 4000 to 1000 cm^{-1} at 25, 100, 200, 350, 400, and 450 °C once steady-state conditions were reached.

2.5. Computational Methods. Periodic DFT calculations were performed using the Perdew–Burke–Ernzenhof (PBE) exchange-correlation functional[48] as implemented in the Vienna Ab initio Simulation Package (VASP) code, version 5.4.4.[49,50] Projector augmented wave (PAW) potentials[51] were used to describe the core electrons of Ce, Ru, O, C, and H ions, while plane waves with a kinetic cutoff energy of 500 eV were employed to represent their valence electrons. For Ce atoms, an additional on-site correction for the electrons localized in the 4f orbital was introduced using an effective Hubbard U term (U_{eff}) of 4.5 eV following Dudarev's approach.[52]

The CeO_2 and metal Ru metal bulk structures were optimized with a Γ-centered Monkhorst–Pack k-point grid of 7 × 7 × 7 and 11 × 11 × 11, respectively, and the equilibrium lattice parameter was calculated using the Birch–Murnaghan equation of state. The most stable facets, *i.e.*, $CeO_2(111)$ and $Ru(0001)$,[53,54] were modeled as surface slabs with at least a 15 Å vacuum gap in the perpendicular direction to the surface to avoid the interaction between the top and bottom layers. The $CeO_2(111)$ and $Ru(0001)$ slabs were built with a periodicity of $p(2 × 2)$, consisting of three and four metal layers, respectively. In both cases, the two upper layers were allowed to relax optimizing the structure using a k-point mesh of 3 × 3 × 1 and 7 × 7 × 1, respectively. The $CeO_2(111)$ and $Ru(0001)$ slabs were constituted by three and four metal layers, respectively. Once optimized, the adsorption energies, ΔE_{ads}, of the CO_2 methanation intermediates were computed as

$$\Delta E_{ads} = E_{ads+slab} - (E_{slab} + E_{ads}) \quad (2)$$

where E_{slab} is the energy of the clean slab, E_{ads} is the energy of the adsorbate species in the gas phase, and $E_{ads+slab}$ is the energy of the slab with the specific adsorbates in the most favorable configuration. These values were employed to calculate the Gibbs adsorption energies, ΔG_{ads}, using the following equation

$$\Delta G_{ads}(T, p_0) = \Delta E_{ads} + \Delta E_{ZPE} - T\Delta S_{ads} \quad (3)$$

where ΔE_{ZPE} and $T\Delta S_{ads}$ denote the changes in zero-point energy and entropy, respectively, relative to the clean slab and the adsorbate molecules in the gas phase. The effect of hydrogen and CO_2 partial pressures on the above Gibbs adsorption energies was introduced as follows

$$\Delta G_{ads}(T, p) = \left[\Delta G_{ads}(T, p_0) - \sum n \cdot \Delta \mu_i(T, p)\right] \quad (4)$$

where $\Delta \mu_i(T, p)$ is the change in chemical potential of the n adsorbed species i at a given temperature and pressure, defined as

$$\Delta \mu_i(T, p) = \Delta \mu_i(T, p_0) + \alpha \cdot k_B T \ln(p_i/p_0) \quad (5)$$

where k_B is the Boltzmann constant, α is taken as 1/2 for H_2 and 1 for CO_2, and $\Delta \mu_i(T, p_0)$ is the change in chemical potential for H_2 or CO_2 at a given temperature and standard pressure.

After assessing the resting state of the $Ru(0001)$ and $CeO_x(111)$ surfaces in the representative thermodynamic reactions conditions, the CO_2 mechanism was investigated by computing the relative energies of the most plausible reaction intermediates on each surface, leading to different reaction pathways. Transition states (TS) for the relevant steps were located by means of the climbing image nudge elastic band method (CI-NEB) using at least five images along the reaction coordinate and the limited-memory Broyden–Fletcher–Goldfarb–Shanno (LBFGS) optimizer. The nature of TSs obtained was verified via vibrational frequency analysis using the finite difference method with a displacement of 0.01 Å.

3. RESULTS AND DISCUSSION

3.1. Catalytic Activity. CO_2 methanation tests were conducted in a conventional fixed-bed reactor containing the Ru/CeO_2 catalyst, and the evolution of CO_2 and CH_4 gases produced during the reaction was monitored as shown in Figure 1. Prior to the experiment, the catalyst was pretreated
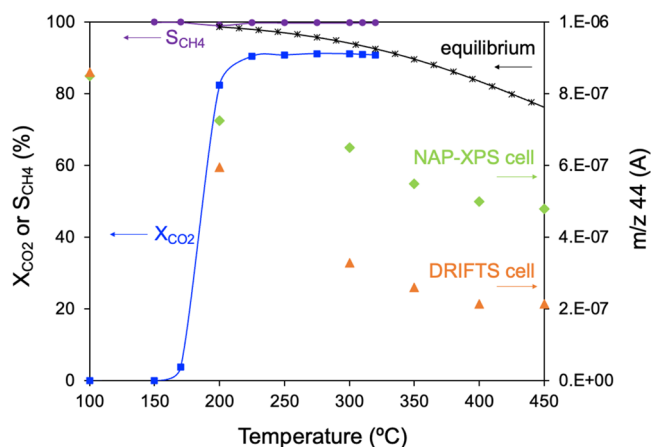

Figure 1. Primary y-axis: CO_2 conversion (X_{CO2}, squares) and CH_4 selectivity (S_{CH4}, circles) as a function of the temperature performed in a fixed-bed conventional reactor. Secondary y-axis: m/z 44 signal measured by mass spectrometry during DRIFTS (triangles) and NAP–XPS experiments (diamonds).

with H_2 at 550 °C for 1 h to reduce the ruthenium species present, in agreement with H_2-TPR profiles (Figure S3). In this experimental setup, the CO_2 methanation activity starts above 170 °C showing a sharp increase in the CO_2 conversion (X_{CO2}) with temperature until a stationary state is achieved at 225 °C. This behavior is similar to that reported in the literature for other Ru/CeO_2 catalysts.[42,43] Notably, only CH_4 and H_2O were detected as reaction products regardless of the temperature, which demonstrates the high selectivity toward

CH_4 relative to other byproducts such as CO. The m/z 44 signal monitored by mass spectrometry during the *in situ* DRIFTS and *in situ* NAP−XPS experiments under CO_2 methanation reaction conditions is also included in Figure 1 for comparison. CO_2 conversion displays similar onsets in the three experimental setups (*ca.* 170 °C), but the effect of temperature on CO_2 consumption is different for each technique. The comparison of the catalytic behavior in the different experimental setups is essential to obtain a meaningful interpretation of experimental results since the reaction conditions used in the conventional fixed-bed reactor are different from those used in spectroscopic experiments (DRIFTS and NAP−XPS) due to the restrictions imposed by the spectroscopy setups.

3.2. In Situ DRIFTS Experiments. Figure 2 shows two relevant wavelength ranges selected from the spectra recorded
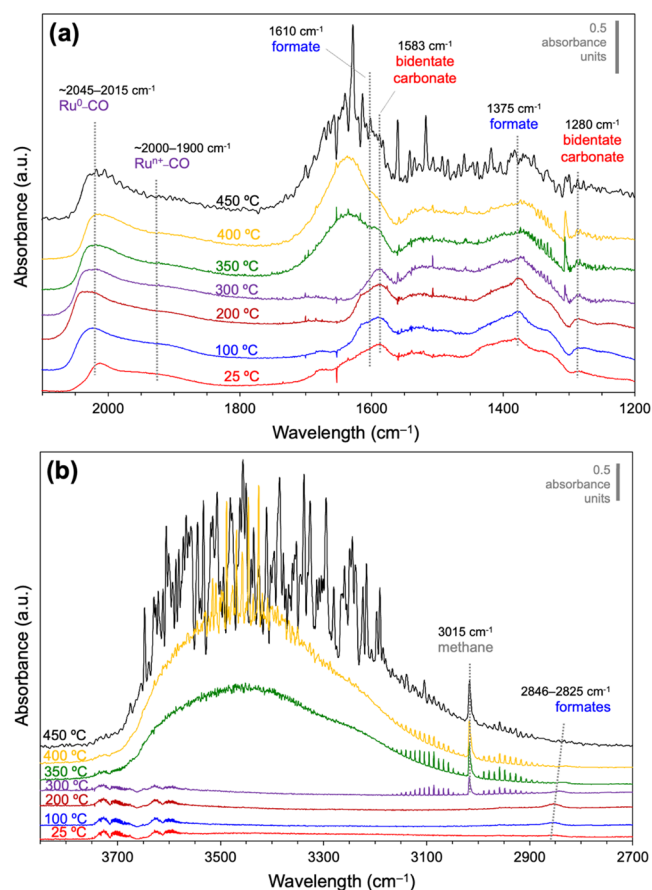
Figure 2. *In situ* DRIFT spectra recorded in steady state under CO_2 methanation gas mixture (CO_2/H_2 1:4) after a reduction pretreatment at 450 °C in H_2/He in the regions: (a) 2100−1200 cm^{-1} and (b) 3800−2700 cm^{-1}.

after steady state was achieved at different temperatures. Figure 2a plots the 2100−1200 cm^{-1} range, which reveals the characteristic bands assigned to different vibration modes of C−O and C═O bonds, where formates (*OCHO) and carbonates (*OCOO) can be discerned, besides the formation of molecular H_2O. The band centered at *ca.* 2000 cm^{-1} is attributed to Ru-carbonyls, showing a lower-wavenumber tail characteristic of their multiple configurations. The linear Ru^0−CO shows between 2045 and 2015 cm^{-1}, while oxidized Ru^{n+}−CO appears at lower wavenumbers.[55] This assignment

contradicts what one would expect due to the lower back-donation from cationic species, but has been elsewhere reported and attributed to lower adsorbate−adsorbate interactions in the oxidized environment.[56] Regarding this, as precisely detailed by Solís-García et al. in a recent paper, we recognize that there is, unfortunately, a large variety and contradictory band assignments on Ru carbonyls in the literature.[57] For instance, according to some studies, bridged zerovalent Ru carbonyls may also be contributing to the broad carbonyl band in the lower-wavenumber region (*i.e.*, 2000−1900 cm^{-1}),[58] although these species have been more frequently reported at *ca.* 1800 cm^{-1}.[59,60] The metallic linear carbonyls display a reversible blueshift to 2045 cm^{-1} attributed to the reduction of their oxidized surface environment by the effect of the reaction mixture followed by a decrease of CO coverage above the methanation onset, setting the Ru^0−CO band back to 2015 cm^{-1}. On the other hand, we do not see a sign of polybonded carbonyls either on metal or cationic Ru sites.

Figure 2b, displaying the 3800−2700 cm^{-1} range, provides information about C−H bonds, including the fingerprint bands of formates, gas-phase CH_4, and O−H vibration bands assigned to surface hydroxyls and water.

Figure 2 proves that CO_2 is chemisorbed on the reduced catalyst at room temperature, as seen by the formation of bidentate carbonates (1583 and 1280 cm^{-1} bands), formates (2846, 1610, and 1375 cm^{-1} bands), and Ru-carbonyls. Carbonates are formed upon CO_2 chemisorption on metal oxides and are assumed to sit on the ceria surface as ruthenium is mostly reduced according to H_2-TPR experiments (Figure S3). Notably, the presence of formates at 25 °C indicates that partial hydrogenation of the chemisorbed CO_2 takes place at room temperature. The H atom in the formate species (*OCHO) can be sourced from either the dissociated H_2 on the catalyst after reduction at 450 °C, presumably on Ru^0, or the hydroxyl groups formed on ceria.[61,62] Isolated hydroxyls are observed in the 25−300 °C range in the spectra as weak bands in the 3750−3600 cm^{-1} region, which are eventually masked below the broad and intense absorption band of polybonded OH or surface H_2O. Since the consumption of hydroxyls is not detected, the first hypothesis regarding the generation of formates is more likely. We also note that the formation of Ru-carbonyls involves the dissociation of the CO_2 molecule, which occurs on the reduced catalyst even at room temperature, despite the methanation reaction onset in this experimental setup is only observed at higher temperatures (see Figure 1). From the DRIFT spectra, however, it is not possible to discern whether CO_2 splits directly onto the Ru particles or the CeO_2 surface followed by CO spillover to the Ru phase. As stated above, the carbonyl band shape allows us to infer the coexistence of both on Ru^0 and on Ru^{n+} species, although Ru is reduced after H_2 pretreatment. The identification of carbonyls on cationic ruthenium (Ru^{n+}−CO) could be evidence of the partial oxidation of ruthenium upon CO_2 exposure at room temperature. This oxidation can be the result of the direct dissociative CO_2 chemisorption into oxygen atoms and carbonyls. However, this is just a hypothesis since the effect of ceria in keeping Ru oxidized through synergistic interactions cannot be ruled out.

Interestingly, we observed that the increase in temperature has an effect on the intensity of the DRIFTS signals but not on the nature of the surface species observed, as indicated by the presence of bands attributed to carbonyls, formates, and

carbonates. In addition, a sharp peak at 3015 cm^{-1} is observed at temperatures above 300 °C, which we assign to the C—H stretching mode of gas-phase CH$_4$. Similarly, water is detected above 350 °C as indicated by the presence of a broad band in the 3700−3450 cm^{-1} range, corresponding to the symmetric and asymmetric stretching of H-bonded hydroxyl groups.[61] The identification of such broad band can also be related to the presence of large coverages of water on the catalyst surface or the accumulation of water in the reaction chamber as a product of the CO$_2$ methanation reaction. Several bands from the spectra shown in Figure 2 have been selected to monitor the evolution of carbonyls (2015 and 1920 cm^{-1}), formates (2830 cm^{-1}), and carbonates (1280 cm^{-1}) with temperature. Note that the characteristic formate bands within 2930−2850 cm^{-1} exhibit a redshift when temperature is increased, which is attributed to the weakening of the C—H bond due to redox changes in the adsorption site. The evolution of band intensities from the selected signals with temperature is presented in Figure 3.
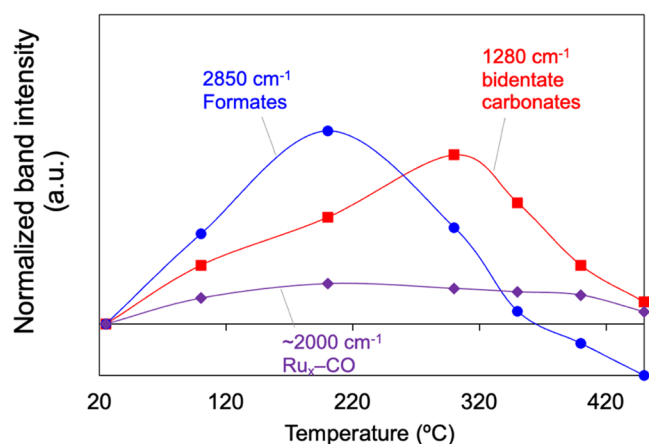

Figure 3. Evolution of formates, bidentate carbonates, and ruthenium carbonyl signals as a function of temperature for the experiments performed in the DRIFTS reactor cell under CO$_2$ methanation gas mixture (10% CO$_2$, 40% H$_2$, 50% He) after a reduction pretreatment at 450 °C with 50% H$_2$/He.

The generation of formates and bidentate carbonates is strongly influenced by the reaction temperature. In particular, their signals peak at 200 and 300 °C, respectively, and then drop. The carbonyl signals also increase slightly from 25 to 200 °C, and then remain constant until 400 °C. This indicates that carbonyls are not only formed on ruthenium at room temperature but also at higher temperatures, and they remain on the catalyst surface even when exposed to CO$_2$ methanation temperatures (above 170 °C). The decrease of the formate, carbonate, and carbonyl bands above *ca.* 200, 300, and 400 °C, respectively, can be attributed to their hydrogenation onset or thermal decomposition. Panagiotopoulou et al.[35] confirmed that Ru-carbonyls are reaction intermediates in the CO$_2$ methanation on Ru/TiO$_2$ catalysts, while other authors[30,63] reached the same conclusion for Ru/Al$_2$O$_3$. However, Wang et al.[43] concluded that formates are the main reaction intermediates. On the contrary, Upham et al.[64] pinpointed carbonates as active intermediates of CO$_2$ methanation while ruling out the participation of CO and formate-type adsorbates in a Ru-doped ceria catalyst with composition Ru$_{0.05}$Ce$_{0.95}$O$_x$. This controversy highlights that particular features of the

ruthenium catalyst and the experimental techniques employed to investigate the CO$_2$ methanation have a major impact on the nature of the intermediates formed and, therefore, the conclusions drawn about the reaction mechanism.

3.3. *In Situ* NAP−XPS Experiments. The spectra recorded under steady-state conditions for Ce 3d and Ru 3d XPS regions are shown in the Supporting Information (see Figures S4 and S5, respectively). From these spectra, the percentages of Ru^0 and Ce^{3+} were calculated,[65] and the results are plotted as a function of temperature in Figures 4 and 5,
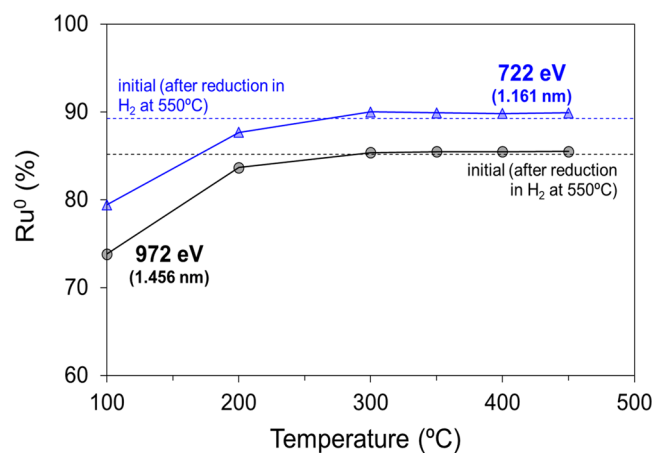

Figure 4. Evolution of Ru^0 content relative to the total ruthenium as measured by NAP−XPS under CO$_2$ methanation gas mixture (10% CO$_2$, 40% H$_2$, 50% N$_2$) after a reduction pretreatment at 550 °C with 50% H$_2$/N$_2$. The photon energies and probed depths (estimated as 3 times the inelastic mean free path, IMFP) are also indicated. These data can be found in the Supporting Information (Table S1) for selected crystalline phases.

respectively. After the reduction pretreatment, NAP−XPS reveals that the surface of the ruthenium catalyst is mainly reduced, with *ca.* 90% Ru^0 as measured with the 722 eV photon energy (see Figure 4 and Table S2). This percentage is
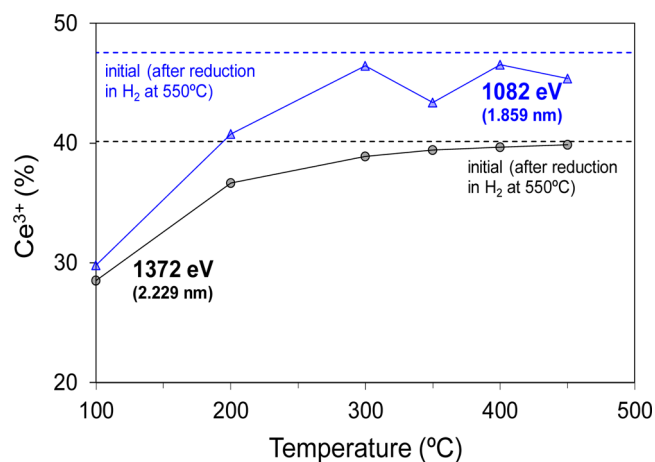
Figure 5. Evolution of Ce^{3+} percentage relative to the total cerium as measured by NAP−XPS under CO$_2$ methanation gas mixture (10% CO$_2$, 40% H$_2$, 50% N$_2$) after a reduction pretreatment at 550 °C with 50% H$_2$/N$_2$. The photon energies and corresponding sample probed depths (estimated as 3 times the IMFP) are also indicated. Data for selected crystalline phases can be found in the Supporting Information (Table S1).
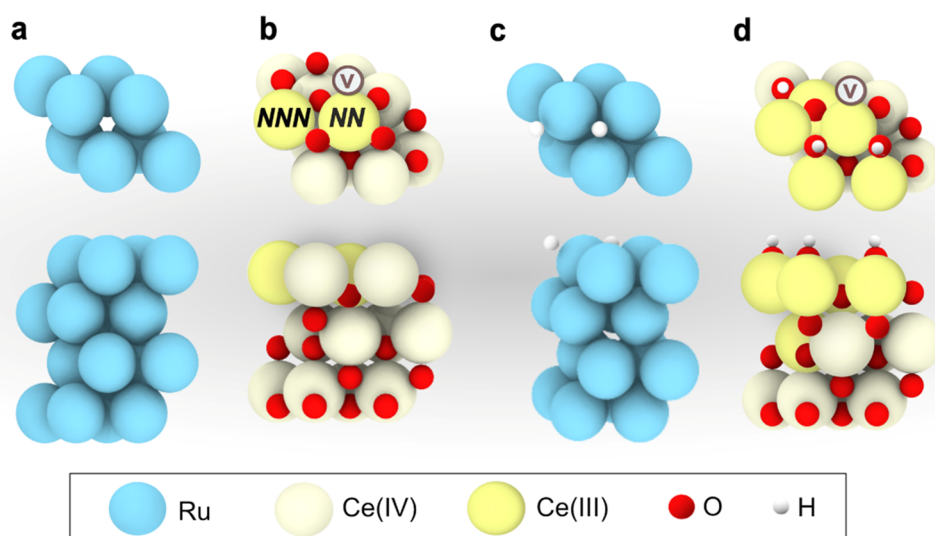
Figure 6. (a) Modeled Ru(0001) and (b) CeO_{2-x}(111) surface slabs. Resting states predicted for (c) Ru(0001) and (d) CeO_{2-x} (111) at 225 °C. O vacancies are denoted with a circled "V".

slightly lower (86%) when probing deeper regions with an incident energy of 972 eV. The presence of surface oxidized Ru after the reduction treatment can be related to the presence of ceria, which promotes the stabilization of oxidized species at the Ru−CeO_2 interface.

The introduction of the methanation reaction gas mixture at 100 °C leads to the oxidation of the ruthenium surface as evidenced by the drop of the Ru^0 percentages from 90 and 86 to 79 and 74% for the 722 and 972 eV incident energies, respectively. This observation is consistent with the dissociative chemisorption of CO_2 leading to Ru-carbonyls and oxygen atoms, which could potentially oxidize partially the surface as observed by DRIFTS. As the temperature increases, the percentages of Ru^0 increase alongside CO_2 consumption up to similar values to those observed during H_2 pretreatment (see Figure 4). Hence, we conclude that the oxygen atoms left on ruthenium upon dissociative chemisorption of CO_2 at low temperatures (*i.e.*, below 200 °C) are removed at higher temperatures in the form of H_2O and/or transferred to ceria.

The percentage of surface Ce^{3+} cations determined by NAP−XPS experiments, shown in Figure 5, amounts to 37% after the reduction pretreatment at 550 °C under H_2, regardless of the probed depth. This percentage decreases when the methanation gas mixture is fed into the reaction cell at 100 °C in accordance with the behavior of ruthenium, evidencing that CO_2 chemisorption oxidizes both ruthenium and ceria. The oxidation of Ce(III) to Ce(IV) under these conditions can occur via the adsorption and dissociation of CO_2 to CO + *O on the reduced surface of ceria, as confirmed by DFT calculations (*vide infra*). According to Figure 5, the change in concentration of Ce^{3+} (from 37% after H_2 pretreatment to 25−14% at 100 °C in CO_2 + H_2) is higher than that for Ru (from 90−86 to 79−74%, respectively, as seen in Figure 4). Hence, considering that there is much more ceria than ruthenium in the Ru/CeO_2 catalyst, we posit that the oxygen generated upon CO_2 dissociation, which goes onto ceria, is much larger than that accumulated on ruthenium, highlighting the key role of ceria as oxygen reservoir.

As observed in Figure 5, increasing the temperature beyond 100 °C leads to the reduction of the ceria surface up to the level achieved with the H_2 reduction pretreatment. The

monitorization of the oxidation state of bulk cerium in a Ru/CeO_2 catalyst under CO_2 methanation conditions using synchrotron radiation was reported by Wang et al.[43] Therein, operando XANES experiments showed that the concentration of Ce^{3+} increased from 3% at room temperature to 9% at 400 °C under reaction conditions. We note that these values are much lower than the ones obtained in this work using NAP−XPS (Figure 5), which we attribute to XANES being a bulk-sensitive analysis while XPS is surface-sensitive.[67] Therefore, we conclude that ceria bulk remains mainly oxidized, whereas the surface is highly reduced (37% Ce^{3+}) at CO_2 methanation temperatures.

In summary, during the CO_2 methanation reaction, the Ru/CeO_2 catalyst is reduced on average with a surface composition of *ca.* 90−86% Ru^0 and 37% Ce^{3+}, which is similar to the catalyst state after the H_2 reduction pretreatment at 550 °C. This indicates that, during CO_2 methanation, the dissociative chemisorption of H_2 is faster than that of CO_2, leading to a larger concentration of H atoms, which most likely remain adsorbed on the ruthenium surface.

3.4. DFT Calculations. *3.4.1. Coverage Analysis and Resting State Assessment.* DFT calculations were carried out to shed light on the CO_2 methanation pathway using representative facets of the Ru/CeO_2 catalyst. Given the polycrystalline nature of the catalyst, as depicted by XRD (Figure S2), the lowest-energy surface slabs were selected and modeled. Namely, Ru(0001) and CeO_2(111), which are inferred to be the most abundant and exposed terminations in the catalyst. The interaction of the surface slabs with the CO_2 + H_2 mixture at representative conditions was studied to assess the participation of each phase in the multistepped reaction mechanism. Because as-prepared ceria is known to exhibit oxygen vacancies, a nonstoichiometric $p(2 \times 2)$-CeO_{2-x}(111) surface with one surface oxygen vacancy was modeled, which corresponds to a 25% surface reduction. The lowest-energy configuration for this slab corresponds to two surface Ce^{3+} ions located in the nearest neighbor (NN) and next-nearest neighbor (NNN) positions relative to the oxygen vacancy, in agreement with previous theoretical studies.[67,68] The modeled Ru(0001) and CeO_{2-x}(111) surface slabs are depicted in Figure 6a,b, respectively.

To assess the catalyst resting state at the onset of the CO_2 methanation reaction, the surface coverage of the $CeO_{2-x}(111)$ and $Ru(0001)$ slabs was investigated by computing the Gibbs adsorption energies of all of the reactant species under relevant experimental conditions (see the Materials and Methods section for details). DFT calculations revealed that the dissociative chemisorption of H_2 on $Ru(0001)$ has a negligible activation barrier (see Figure S6), rendering this process extremely fast. Hence, we focused our coverage analysis of this surface on the computation of the Gibbs energy of consecutive H adsorptions as a function of temperature. The results derived from this analysis led to the prediction of a surface with all of the fcc sites occupied by H atoms as the catalyst resting state at room temperature (Figure S7). In addition, calculations revealed that, as temperature increases, lower H coverages become more stable until the clean surface prevails at temperatures above *ca.* 300 °C. At 225 °C, a temperature slightly above the experimental onset found in methanation catalytic tests (*ca.* 175 °C), the Ru surface is predicted to be partially covered with 2H atoms in fcc positions, as shown in Figure 6a. Hence, this surface termination was selected for the mechanistic studies of the CO_2 methanation reaction on $Ru(0001)$.

Similarly to $Ru(0001)$, H_2 activation on the $CeO_2(111)$ surface has been shown to demand a relatively low energy barrier (*ca.* 1 eV), leading to the hydroxylation of the surface in a highly exergonic process.[57] Consequently, we modeled the $CeO_{2-x}(111)$ surface with different levels of hydroxylation as a function of reaction temperature (Figure S7b), finding a coverage with 3OH groups and 1O vacancy (see Figure 6b) as the most likely surface termination within the experimental temperature range of 25−360 °C. Hence, we selected this surface coverage to investigate the CO_2 methanation mechanism on $CeO_{2-x}(111)$.

3.4.2. CO₂ Methanation on Ru(0001). The binding of a CO_2 molecule was investigated on all possible sites of the $Ru(0001)$ surface. The most favorable adsorption sites are depicted in Figure S8. On the clean $Ru(0001)$ surface, we found that CO_2 is weakly adsorbed in a V-shape on an fcc site with a Gibbs energy of +0.15 eV, while CO_2 adsorption is hampered on the H-covered $Ru(0001)$ surfaces. In particular, CO_2 remains physisorbed at 4.02 Å on the 4H-fcc surface as there are no fcc sites available in this coverage. Hence, a H coverage blocks CO_2 adsorption and only when fcc sites become available at high temperatures, CO_2 can be adsorbed. This remark points out that CO_2 adsorption and activation on Ru can be limited at the initial CO_2 methanation conditions and conditioned by the H coverage.

After determining the 2H-covered $Ru(0001)$ surface as the catalyst resting state under relevant CO_2 methanation conditions, the potential CO_2 evolution pathways were investigated at 225 °C. The lowest Gibbs energy diagrams obtained for the formation of Ru-carbonyls observed in experiments are depicted in Figure 7. These pathways involve the hydrogenation of CO_2 by the surface H atoms followed by the restitution of the H coverage as the dissociative chemisorption of H_2 has been shown to be extremely fast and highly exergonic.

As shown in Figure 7, after CO_2 adsorption on the H-covered surface, CO_2 can either split into *CO and *O or be hydrogenated to other species, namely, formate (*OCHO*, red trace) or hydrocarboxylate (*COOH, green trace). $Ru(0001)$ surfaces displaying high H coverages have been
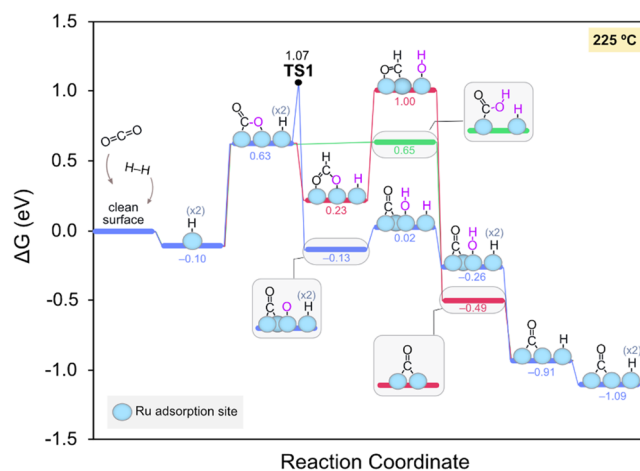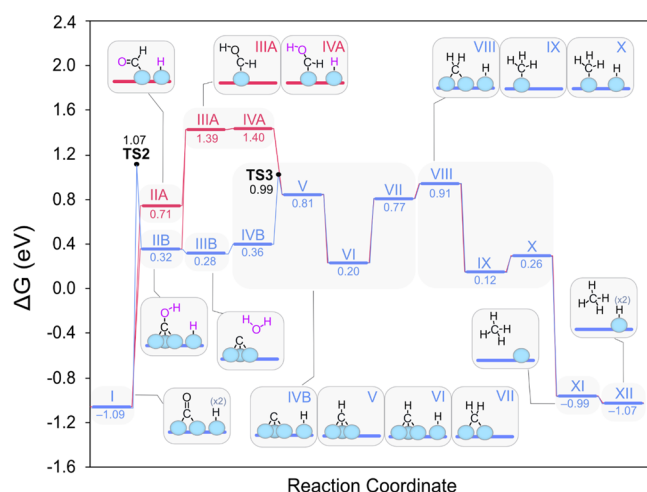

Figure 7. Calculated Gibbs energy diagram for the formation of carbonyl groups on $Ru(0001)$ under CO_2 methanation conditions at 225 °C.

reported to favor CO_2 hydrogenation over CO_2 dissociation since the former frees one active site, whereas the latter requires an additional surface site for the binding of the generated *O.[66] However, because a partial H coverage is predicted under our experimental reaction conditions, we find that CO_2 dissociation is the most thermodynamically favored route by 0.30 eV. This step is also independent of the reaction temperature, as illustrated in Figure S9. DFT calculations indicate that the cleavage of CO_2 is exergonic by −0.70 eV and requires a low relative barrier of 0.44 eV (see Figure S10), rendering this process feasible under experimental conditions. Importantly, we note that this step results in the local reoxidation of Ru due to the adsorption of *O, which is in line with the surface reoxidation observed by NAP−XPS. The presence of carbonyl groups on cationic Ru sites observed in the DRIFT spectra could be explained by means of this mechanism, too. However, although our theoretical findings show that CO_2 split on Ru surfaces is thermodynamically feasible under methanation conditions, it is not accurate to attribute such cationic species to this process since the role of the support in the redox state of the Ru particles cannot be ruled out. After CO_2 dissociation, the *O species is hydrogenated in two consecutive steps to form an *OH group and then H_2O, which desorbs from the surface reducing Ru back to its original state.

Notably, this mechanism is considerably lower in energy than the alternative paths involving formates and their evolution via hydrocarboxylates (*COOH) or formyl groups (*CHO), which can also lead to very stable *CO groups by releasing water to the gas phase, as shown in Figure 7. This is also in line with the broad and intense $Ru^{n+}-CO$ band detected in in situ DRIFTS experiments all along the reaction course. Overall, Figure 7 shows that Ru-carbonyls are very stable and that these can be formed via different pathways, although the CO_2 dissociative route is predicted to dominate. This may explain the broad and irregular shape of the carbonyl band in the DRIFT spectra, indicating the accumulation of CO in different local environments on the surface.

Once the stable *CO species has been formed on the $Ru(0001)$ surface, these can be hydrogenated to *COH or *CHO, which have been proposed to be further hydrogenated to CH_4 in a rate-determining process.[66] As can be observed in Figure 8, our calculations indicate that CO hydrogenation to
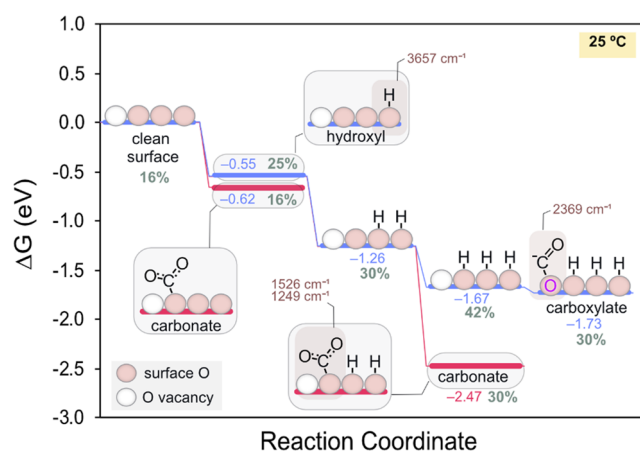
Figure 8. Calculated Gibbs energies for different CO evolution pathways on Ru(0001) under methanation conditions at 225 °C.

Figure 9. Calculated Gibbs energies at 25 °C for the most favorable adsorption modes of CO_2 on the $CeO_{2-x}(111)$ surface with 1O vacancy under the predicted H coverage. Computed vibrational frequencies are shown in brown, while the % Ce^{3+} in the $CeO_{2-x}(111)$ surfaces is displayed in gray.

*COH is more favorable by *ca.* 0.40 eV and demands an energy barrier of 2.16 eV (see Figure S11 for the TS2 calculation), which is considerably higher than that for CO_2 dissociation. This observation could explain the carbonyl formation at room temperature and their constant concentration on surface up to 400 °C. Subsequently, *COH undergoes hydrogenation to *C and H_2O, which desorbs into the gas phase in an almost thermoneutral process. From this point, the adsorbed *C evolves as the final product CH_4 through consecutive hydrogenations involving exergonic or moderately endergonic steps. One of the endergonic steps of the mechanism corresponds to the hydrogenation of *C to *CH, although this process exhibits a relative energy barrier of only 0.63 eV (difference between TS3 and IVB). Therefore, we assume low comparable barriers for the successive stepwise hydrogenations.

Overall, because of the marked stability of the Ru-carbonyls, we conclude that *CO to CH_4 hydrogenation requires a global activation energy of *ca.* 2.0 eV, which corresponds to the formation of *COH via TS2. This high energy barrier is in good agreement with *in situ* experimental DRIFTS, which shows that the Ru−CO band is already intense at room temperature and remains unaltered throughout the reaction course. In addition, there is no sign of CO_2 conversion at temperatures below the CO_2 methanation onset and no CO is detected in the outlet streams, pointing to *CO hydrogenation as the RDS. Hence, both experiments and theoretical studies indicate that CO is strongly bound on Ru(0001), where it accumulates until the temperature is high enough (CO_2 methanation onset is at *ca.* 175 °C) to hydrogenate *CO to CH_4. The effect of temperature is observed in Figure S9, where the most favored mechanistic route remains the same at 425 °C. In conclusion, *CO adsorbs on the H-covered Ru(0001), the first hydrogenation takes place, and the formation of subsequent intermediates is thermodynamically driven.

3.4.3. CO_2 Methanation on $CeO_{2-x}(111)$. After modeling the CO_2 methanation mechanism on Ru(0001), we turned our attention to ceria using the resting state predicted above with 3OH groups and 1O vacancy.

In contrast to Ru, CeO_2 has good affinity for CO_2 retention,[69,70] which further grows with the presence of reduced Ce^{3+} cations. As shown in Figure 9, the binding of CO_2 onto a surface oxygen to form a carbonate species

(*OCOO) is exergonic by −0.62 eV on the reduced surface. However, we note that, in the presence of H_2, these two processes can compete since both hydroxylation and carbonate formation require an available surface oxygen. Interestingly, unlike with Ru(0001), the presence of surface OH groups favors the formation of carbonates. In fact, the 2*OH + *OCOO state is more stable than the coverage with only 3*OH (−2.47 vs −1.67 eV). Therefore, *OCOO and *OH groups are expected to coexist on ceria, in good agreement with DRIFTS. Alternatively, CO_2 can also bind on the oxygen vacancy site in the 3*OH surface as a V-shaped carboxylate species with an energy of −1.73 eV. This adsorption mode is especially relevant since the oxygen vacancy is partially refilled by one of the oxygen atoms from CO_2, leading to the reoxidation of ceria as observed by NAP−XPS. These carboxylates may evolve in two different pathways as shown in the Gibbs energy diagram presented in Figure 10, namely, via direct splitting into CO and O, which directly refills the oxygen vacancy (red trace), or through the hydrogenation to formates (blue trace).

We note that the resulting CO released via the carboxylate route is not chemisorbed on ceria according to DFT calculations, neither released to the gas phase since no CO
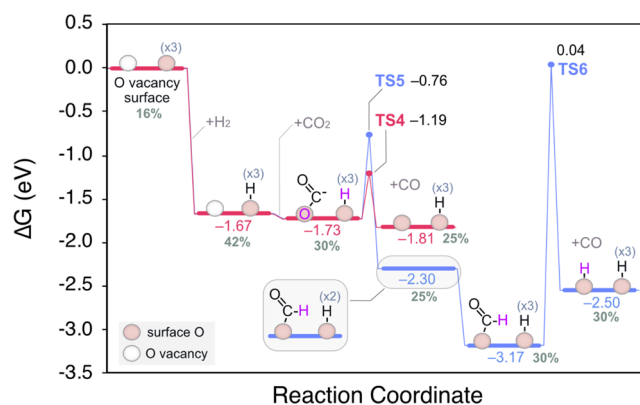
Figure 10. Calculated Gibbs energy diagram for the formation of carboxylates and their decomposition pathways at 25 °C. The % Ce^{3+} on the slab at each reaction step is shown in gray.

was detected in the outlet gases. Therefore, it is very likely that the weakly physisorbed CO interacts with the Ru phase at the triple-phase boundary of the Ru/CeO$_2$ catalyst giving rise to Ru-carbonyls. Nonetheless, given the low energy barrier (TS4) found for the splitting of carboxylates on ceria (0.54 eV; see Figure S13), we conclude that carboxylates are a potential additional source of Ru-carbonyls at room temperature.

Our calculations also predict that carboxylates can be largely stabilized as formates with a slightly larger activation energy of 0.97 eV via TS5 (see Figure S14) and remain on surface until sufficient energy is provided for their decomposition into CO (Figure 10, blue trace). Importantly, while formates are thermodynamically much more stable than carboxylates, they are predicted to be rather kinetically inert, in agreement with the observation of the depletion of the formates band in DRIFTs above 200 °C. Finally, in contrast to formates, carbonates may be merely released as CO$_2$ as the temperature increases, whose depletion is triggered beyond 300 °C according to DRIFTS.

Overall, theoretical calculations reveal that ceria can source CO to the ruthenium catalyst at low and high temperatures, giving rise to Ru-carbonyls in addition to the intrinsic capacity of Ru to split CO$_2$ with a moderate activation energy. This highlights the important role of ceria as an oxygen sink by assisting in the Ru-catalyzed reaction mechanism, which is not possible with inert supports like Al$_2$O$_3$ or SiO$_2$ rendering a poorer catalytic performance. Besides, these results shed light on why Ru/CeO$_2$ catalysts with Ru and CeO$_2$ phases in tight interaction exhibit improved catalytic performance for the CO$_2$ methanation reaction, in good agreement with experiments. Simulations show that Ru on its own can promote both H$_2$ dissociation and CO$_2$ methanation, while the ceria support facilitates CO$_2$ dissociation. Since the binding of CO$_2$ on Ru metal is weak and even more difficult on the H-covered surface, the assistance of ceria is very beneficial to accelerate the CO$_2$ methanation rate at temperatures around the reaction onset. Future modeling studies of the Ru−Ce interfacial sites should confirm the key role of synergistic interactions arising in Ru-supported cerium oxide catalysts.

4. CONCLUSIONS

This work has investigated the catalytic behavior of a high-performance Ru/CeO$_2$ catalyst on the CO$_2$ methanation reaction by means of *in situ* spectroscopic techniques and periodic DFT calculations of the individual Ru and CeO$_2$ phases under representative reaction conditions. Exposure of the CO$_2$ + H$_2$ methanation mixture on the Ru metal and CeO$_2$ results in the partial reoxidation of these surfaces via CO$_2$ dissociative chemisorption at room temperature, as confirmed by NAP−XPS. The CO$_2$ chemisorption on both Ru and CeO$_2$ modeled by DFT supports the oxidative nature of the process.

H$_2$ activation and dissociation under CO$_2$ methanation conditions can occur on both the Ru phase, in an almost barrierless process, and on CeO$_{2−x}$(111), with a low activation energy, leading to high H and OH coverages, respectively. For ceria, surface hydroxylation is beneficial for CO$_2$ retention, while the opposite is predicted for Ru. This complementarity seems to have a positive influence on the overall reactivity, enabling additional CO$_2$ adsorption sites which are predicted to be accessible to Ru at the Ru/CeO$_2$ interface. The overall rate-determining step in the CO$_2$ methanation mechanism on the Ru/CeO$_2$ catalyst is the hydrogenation of Ru-carbonyls with an energy barrier of 2.16 eV.

On ceria, we have shown that CO$_2$ is accumulated on the surface in the form of strongly bound carbonates, while carboxylates sitting on oxygen vacancies are thermodynamically driven to the generation of formate species. The evolution of the latter stable species requires a considerable activation energy, and hence, they remain adsorbed on the ceria surface up to 200 °C. Beyond this temperature, formates can decompose to CO and yield ruthenium carbonyls, as observed by DRIFTS. On the other hand, at lower temperatures, carboxylates are kinetically very reactive leading to CO and O*, restoring the oxygen vacancy and giving rise to the Ru-carbonyls observed at room temperature via a spillover mechanism.

Although Ru shows a very weak CO$_2$ binding unlike CeO$_2$, an incipient Ru reoxidation is also observed in CO$_2$ methanation reaction conditions even at room temperature. This Ru oxidation must be related to the synergistic Ru−CeO$_2$ interactions, either by O spillover from ceria at the interfacial sites or by enabling highly active interfacial sites, which split CO$_2$ and stabilize CO very strongly.

■ ASSOCIATED CONTENT

Ⓢ Supporting Information

■ AUTHOR INFORMATION

Corresponding Authors

Arantxa Davó-Quiñonero − *Departamento de Química Inorgánica, Universidad de Alicante, E-03080 Alicante, Spain; School of Chemistry, CRANN and AMBER Research Centres, Trinity College Dublin, Dublin 2, Ireland;* orcid.org/0000-0001-9776-3458; Email: arantxa.davo@tcd.ie

Max García-Melchor − *School of Chemistry, CRANN and AMBER Research Centres, Trinity College Dublin, Dublin 2, Ireland;* orcid.org/0000-0003-1348-4692; Email: garciamm@tcd.ie

Agustín Bueno-López − *Departamento de Química Inorgánica, Universidad de Alicante, E-03080 Alicante, Spain;* orcid.org/0000-0002-5434-6459; Email: agus@ua.es

Authors

Sergio López-Rodríguez − *Departamento de Química Inorgánica, Universidad de Alicante, E-03080 Alicante, Spain*

Esther Bailón-García − *Departamento de Química Inorgánica, Universidad de Alicante, E-03080 Alicante, Spain;* orcid.org/0000-0001-8418-8714

Dolores Lozano-Castelló − *Departamento de Química Inorgánica, Universidad de Alicante, E-03080 Alicante, Spain*

Facundo C. Herrera − *ALBA Synchrotron Light Source, 08290 Barcelona, Spain; Instituto de Investigaciones Fisicoquímicas Teóricas y Aplicadas (INIFTA, CONICET), Departamento de Química, Facultad de Ciencias Exactas, Universidad Nacional de La Plata, 1900 La Plata, Argentina*

Eric Pellegrin − *ALBA Synchrotron Light Source, 08290 Barcelona, Spain; Present Address: Carl Zeiss SMT GmbH, Rudolf-Eber-Straße. 2, 73447 Ober-kochen, Germany*

Carlos Escudero − *ALBA Synchrotron Light Source, 08290 Barcelona, Spain;* ⊙ orcid.org/0000-0001-8716-9391

Complete contact information is available at:
https://pubs.acs.org/10.1021/acs.jpcc.1c07537

Author Contributions

The manuscript was written through contributions of all authors. All authors have given approval to the final version of the manuscript. All authors contributed equally.

Notes

The authors declare no competing financial interest.

■ REFERENCES

(1) European Commission. Energy Roadmap 2050 (2011). https://ec.europa.eu/energy/sites/ener/files/documents/2012_energy_roadmap_2050_en_0.pdf (accessed October, 2020).

(2) United Nations Framework Convention on Climate Change. Paris Agreement (2015). https://unfccc.int/files/essential_background/convention/application/pdf/english_paris_agreement.pdf (accessed October, 2020).

(3) Sverko Grdic, Z.; Krstinic Nizic, M.; Rudan, E. Circular Economy Concept in the Context of Economic Development in EU Countries. *Sustainability* **2020**, *12*, 3060−3073.

(4) Wang, N.; Guo, Z.; Meng, F.; Wang, H.; Yin, J.; Liu, Y. The Circular Economy and Carbon Footprint: A Systematic Accounting for Typical Coal-Fuelled Power Industrial Parks. *J. Cleaner Prod.* **2019**, *229*, 1262−1273.

(5) Schiebahn, S.; Grube, T.; Robinius, M.; Tietze, V.; Kumar, B.; Stolten, D. Power to Gas: Technological Overview, Systems Analysis and Economic Assessment for a Case Study in Germany. *Int. J. Hydrogen Energy* **2015**, *40*, 4285−4294.

(6) Götz, M.; Lefebvre, J.; Mörs, F.; McDaniel Koch, A.; Graf, F.; Bajohr, S.; Reimert, R.; Kolb, T. Renewable Power-to-Gas: A Technological and Economic Review. *Renewable Energy* **2016**, *85*, 1371−1390.

(7) Velazquez Abad, A.; Dodds, P. E. Green Hydrogen Characterisation Initiatives: Definitions, Standards, Guarantees of Origin, and Challenges. *Energy Policy* **2020**, *138*, 111300−111313.

(8) Gondal, I. A. Offshore Renewable Energy Resources and Their Potential in a Green Hydrogen Supply Chain through Power-to-Gas. *Sustainable Energy Fuels* **2019**, *3*, 1468−1489.

(9) Lee, W. J.; Li, C.; Prajitno, H.; Yoo, J.; Patel, J.; Yang, Y.; Lim, S. Recent Trend in Thermal Catalytic Low Temperature CO_2 Methanation: A Critical Review. *Catal. Today* **2021**, *368*, 2−19.

(10) Alcalde-Santiago, V.; Davó-Quiñonero, A.; Lozano-Castelló, D.; Quindimil, A.; De-La-Torre, U.; Pereda-Ayo, B.; González-Marcos, J. A.; González-Velasco, J. R.; Bueno-López, A. Ni/LnOx Catalysts (Ln=La, Ce or Pr) for CO_2 Methanation. *ChemCatChem* **2018**, *11*, 810−819.

(11) Frontera, P.; Macario, A.; Ferraro, M.; Antonucci, P. L. Supported Catalysts for CO_2 Methanation: A Review. *Catalysts* **2017**, *7*, 59−87.

(12) Li, Z.; Zhao, T.; Zhang, L. Promotion Effect of Additive Fe on Al_2O_3 Supported Ni Catalyst for CO_2 Methanation. *Appl. Organomet. Chem.* **2018**, *32*, No. e4328.

(13) Lin, J.; Ma, C.; Luo, J.; Kong, X.; Xu, Y.; Ma, G.; Wang, J.; Zhang, C.; Li, Z.; Ding, M. Preparation of Ni Based Mesoporous Al_2O_3 Catalyst with Enhanced CO_2 Methanation Performance. *RSC Adv.* **2019**, *9*, 8684−8694.

(14) Moghaddam, S. V.; Rezaei, M.; Meshkani, F.; Daroughegi, R. Synthesis of Nanocrystalline Mesoporous $Ni/Al_2O_3SiO_2$ Catalysts for CO_2 Methanation Reaction. *Int. J. Hydrogen Energy* **2018**, *43*, 19038−19046.

(15) Van Herwijnen, T.; Van Doesburg, H.; De Jong, W. A. Kinetics of the Methanation of CO and CO_2 on a Nickel Catalyst. *J. Catal.* **1973**, *28*, 391−402.

(16) Zhan, Y.; Wang, Y.; Gu, D.; Chen, C.; Jiang, L.; Takehira, K. $Ni/Al2O_3-ZrO_2$ Catalyst for CO_2 Methanation: The Role of γ-(Al, Zr)$_2$O$_3$ Formation. *Appl. Surf. Sci.* **2018**, *459*, 74−79.

(17) Zhang, Z.; Tian, Y.; Zhang, L.; Hu, S.; Xiang, J.; Wang, Y.; Xu, L.; Liu, Q.; Zhang, S.; Hu, X. Impacts of Nickel Loading on Properties, Catalytic Behaviors of $Ni/\gamma−Al_2O_3$ Catalysts and the Reaction Intermediates Formed in Methanation of CO_2. *Int. J. Hydrogen Energy* **2019**, *44*, 9291−9306.

(18) Bian, Z.; Chan, Y. M.; Yu, Y.; Kawi, S. Morphology Dependence of Catalytic Properties of Ni/CeO_2 for CO_2 Methanation: A Kinetic and Mechanism Study. *Catal. Today* **2020**, *347*, 31−38.

(19) Konishcheva, M. V.; Potemkin, D. I.; Badmaev, S. D.; Snytnikov, P. V.; Paukshtis, E. A.; Sobyanin, V. A.; Parmon, V. N. On the Mechanism of CO and CO_2 Methanation Over Ni/CeO_2 Catalysts. *Top. Catal.* **2016**, *59*, 1424−1430.

(20) Tada, S.; Shimizu, T.; Kameyama, H.; Haneda, T.; Kikuchi, R. Ni/CeO_2 Catalysts with High CO_2 Methanation Activity and High CH_4 Selectivity at Low Temperatures. *Int. J. Hydrogen Energy* **2012**, *37*, 5527−5531.

(21) Zhou, G.; Liu, H.; Cui, K.; Xie, H.; Jiao, Z.; Zhang, G.; Xiong, K.; Zheng, X. Methanation of Carbon Dioxide over Ni/CeO_2 Catalysts: Effects of Support CeO_2 Structure. *Int. J. Hydrogen Energy* **2017**, *42*, 16108−16117.

(22) Jacquemin, M.; Beuls, A.; Ruiz, P. Catalytic Production of Methane from CO_2 and H_2 at Low Temperature: Insight on the Reaction Mechanism. *Catal. Today* **2010**, *157*, 462−466.

(23) Karelovic, A.; Ruiz, P. Mechanistic Study of Low Temperature CO_2 Methanation over Rh/TiO_2 Catalysts. *J. Catal.* **2013**, *301*, 141−153.

(24) Panagiotopoulou, P. Hydrogenation of CO_2 over Supported Noble Metal Catalysts. *Appl. Catal., A* **2017**, *542*, 63−70.

(25) Sápi, A.; Rajkumar, T.; Ábel, M.; Efremova, A.; Grósz, A.; Gyuris, A.; Ábrahámné, K. B.; Szenti, I.; Kiss, J.; Varga, T.; et al. Noble-Metal-Free and Pt Nanoparticles-Loaded, Mesoporous Oxides

as Efficient Catalysts for CO_2 Hydrogenation and Dry Reforming with Methane. *J. CO2 Util.* **2019**, *32*, 106−118.

(26) Zamani, A. H.; Ali, R.; Abu Bakar, W. A. W. Optimization of CO_2 Methanation Reaction over M*/Mn/Cu−Al_2O_3 (M*: Pd, Rh and Ru) Catalysts. *J. Ind. Eng. Chem.* **2015**, *29*, 238−248.

(27) Zhang, Z.; Zhang, L.; Hülsey, M. J.; Yan, N. Zirconia Phase Effect in Pd/ZrO_2 Catalyzed CO_2 Hydrogenation into Formate. *Mol. Catal.* **2019**, *475*, 110461−110469.

(28) Abdel-Mageed, A. M.; Widmann, D.; Olesen, S. E.; Chorkendorff, I.; Behm, R. J. Selective CO Methanation on Highly Active Ru/TiO_2 Catalysts: Identifying the Physical Origin of the Observed Activation/Deactivation and Loss in Selectivity. *ACS Catal.* **2018**, *8*, 5399−5414.

(29) Dreyer, J. A. H.; Li, P.; Zhang, L.; Beh, G. K.; Zhang, R.; Sit, P. H.-L.; Teoh, W. Y. Influence of the Oxide Support Reducibility on the CO_2 Methanation over Ru-Based Catalysts. *Appl. Catal., B* **2017**, *219*, 715−726.

(30) Falbo, L.; Visconti, C. G.; Lietti, L.; Szanyi, J. The Effect of CO on CO_2 Methanation over Ru/Al_2O_3 Catalysts: A Combined Steady-State Reactivity and Transient DRIFT Spectroscopy Study. *Appl. Catal., B* **2019**, *256*, 117791−117803.

(31) Mohamed, Z.; Dasireddy, V. D. B. C.; Singh, S.; Friedrich, H. B. TiO_2 and ZrO_2 Supported Ru Catalysts for CO Mitigation Following the Water-Gas Shift Reaction. *Int. J. Hydrogen Energy* **2018**, *43*, 22291−22302.

(32) Muñoz-Murillo, A.; Martínez, T.; Domínguez, M. I.; Odriozola, J. A.; Centeno, M. A. Selective CO Methanation with Structured RuO_2/Al_2O_3 Catalysts. *Appl. Catal., B* **2018**, *236*, 420−427.

(33) Navarro-Jaén, S.; Navarro, J. C.; Bobadilla, L. F.; Centeno, M. A.; Laguna, O. H.; Odriozola, J. A. Size-Tailored Ru Nanoparticles Deposited over γ-Al_2O_3 for the CO_2 Methanation Reaction. *Appl. Surf. Sci.* **2019**, *483*, 750−761.

(34) Nguyen, H. T. T.; Kumabe, Y.; Ueda, S.; Kan, K.; Ohtani, M.; Kobiro, K. Highly Durable Ru Catalysts Supported on CeO_2 Nanocomposites for CO_2 Methanation. *Appl. Catal., A* **2019**, *577*, 35−43.

(35) Petala, A.; Panagiotopoulou, P. Methanation of CO_2 over Alkali-Promoted Ru/TiO_2 Catalysts: I. Effect of Alkali Additives on Catalytic Activity and Selectivity. *Appl. Catal., B* **2018**, *224*, 919−927.

(36) Porta, A.; Falbo, L.; Visconti, C. G.; Lietti, L.; Bassano, C.; Deiana, P. Synthesis of Ru-Based Catalysts for C_{O2} Methanation and Experimental Assessment of Intraporous Transport Limitations. *Catal. Today* **2020**, *343*, 38−47.

(37) Avanesian, T.; Gusmão, G. S.; Christopher, P. Mechanism of CO_2 Reduction by H_2 on Ru(0001) and General Selectivity Descriptors for Late-Transition Metal Catalysts. *J. Catal.* **2016**, *343*, 86−96.

(38) Vogt, C.; Groeneveld, E.; Kamsma, G.; Nachtegaal, M.; Lu, L.; Kiely, C. J.; Berben, P. H.; Meirer, F.; Weckhuysen, B. M. Unravelling Structure Sensitivity in CO_2 Hydrogenation over Nickel. *Nat. Catal.* **2018**, *1*, 127−134.

(39) Frei, M. S.; Mondelli, C.; García-Muelas, R.; Morales-Vidal, J.; Philipp, M.; Safonova, O. V.; López, N.; Stewart, J. A.; Ferré, D. C.; Pérez-Ramírez, J. Nanostructure of Nickel-Promoted Indium Oxide Catalysts Drives Selectivity in CO_2 Hydrogenation. *Nat. Commun.* **2021**, *12*, 1960.

(40) Miao, B.; Ma, S. S. K.; Wang, X.; Su, H.; Chan, S. H. Catalysis Mechanisms of CO_2 and CO Methanation. *Catal. Sci. Technol.* **2016**, *6*, 4048−4058.

(41) Proaño, L.; Tello, E.; Arellano-Trevino, M. A.; Wang, S.; Farrauto, R. J.; Cobo, M. In-Situ DRIFTS Study of Two-Step CO_2 Capture and Catalytic Methanation over Ru,"Na_2O"/Al_2O_3 Dual Functional Material. *Appl. Surf. Sci.* **2019**, *479*, 25−30.

(42) Wang, F.; Li, C.; Zhang, X.; Wei, M.; Evans, D. G.; Duan, X. Catalytic Behavior of Supported Ru Nanoparticles on the {100}, {110}, and {111} Facet of CeO_2. *J. Catal.* **2015**, *329*, 177−186.

(43) Wang, F.; He, S.; Chen, H.; Wang, B.; Zheng, L.; Wei, M.; Evans, D. G.; Duan, X. Active Site Dependent Reaction Mechanism over Ru/CeO_2 Catalyst toward CO_2 Methanation. *J. Am. Chem. Soc.* **2016**, *138*, 6298−6305.

(44) Tada, S.; Ochieng, O. J.; Kikuchi, R.; Haneda, T.; Kameyama, H. Promotion of CO_2 Methanation Activity and CH_4 Selectivity at Low Temperatures over Ru/CeO_2/Al_2O_3 Catalysts. *Int. J. Hydrogen Energy* **2014**, *39*, 10090−10100.

(45) Toemen, S.; Abu Bakar, W. A. W.; Ali, R. Effect of Ceria and Strontia over Ru/Mn/Al_2O_3 Catalyst: Catalytic Methanation, Physicochemical and Mechanistic Studies. *J. CO2 Util.* **2016**, *13*, 38−49.

(46) Pérez-Dieste, V.; Aballe, L.; Ferrer, S.; Nicolàs, J.; Escudero, C.; Milán, A.; Pellegrin, E. Near Ambient Pressure XPS at ALBA. *J. Phys. Conf. Ser.* **2013**, *425*, No. 072023.

(47) Tanuma, S.; Powell, C. J.; Penn, D. R. Calculations of Electron Inelastic Mean Free Paths. V. Data for 14 Organic Compounds over the 50−2000 EV Range. *Surf. Interface Anal.* **1994**, *21*, 165−176.

(48) Perdew, J. P.; Burke, K.; Ernzerhof, M. Generalized Gradient Approximation Made Simple. *Phys. Rev. Lett.* **1996**, *77*, 3865−3868.

(49) Kresse, G.; Furthmüller, J. Efficiency of Ab-Initio Total Energy Calculations for Metals and Semiconductors Using a Plane-Wave Basis Set. *Comput. Mater. Sci.* **1996**, *6*, 15−50.

(50) Kresse, G.; Furthmüller, J. Efficient Iterative Schemes for Ab Initio Total-Energy Calculations Using a Plane-Wave Basis Set. *Phys. Rev. B* **1996**, *54*, 11169−11186.

(51) Blöchl, P. E. Projector Augmented-Wave Method. *Phys. Rev. B* **1994**, *50*, 17953−17979.

(52) Dudarev, S. L.; Botton, G. A.; Savrasov, S. Y.; Humphreys, C. J.; Sutton, A. P. Electron-Energy-Loss Spectra and the Structural Stability of Nickel Oxide: An LSDA+U Study. *Phys. Rev. B* **1998**, *57*, 1505−1509.

(53) Nolan, M.; Grigoleit, S.; Sayle, D. C.; Parker, S. C.; Watson, G. W. Density Functional Theory Studies of the Structure and Electronic Structure of Pure and Defective Low Index Surfaces of Ceria. *Surf. Sci.* **2005**, *576*, 217−229.

(54) Vitos, L.; Ruban, A. V.; Skriver, H. L.; Kollár, J. The Surface Energy of Metals. *Surf. Sci.* **1998**, *411*, 186−202.

(55) Panagiotopoulou, P.; Verykios, X. E. Mechanistic Study of the Selective Methanation of CO over Ru/TiO2 Catalysts: Effect of Metal Crystallite Size on the Nature of Active Surface Species and Reaction Pathways. *J. Phys. Chem. C* **2017**, *121*, 5058−5068.

(56) Elmasides, C.; Kondarides, D. I.; Grünert, W.; Verykios, X. E. XPS and FTIR Study of Ru/Al_2O_3 and Ru/TiO_2 Catalysts: Reduction Characteristics and Interaction with a Methane−Oxygen Mixture. *J. Phys. Chem. B* **1999**, *103*, 5227−5239.

(57) Solís-García, A.; Zepeda, T. A.; Fierro-González, J. C. Spectroscopic Evidence of Surface Species during CO_2 Methanation Catalyzed by Supported Metals: A Review. *Catal. Today* **2021**, *368*, 2.

(58) Bobadilla, L. F.; Garcilaso, V.; Centeno, M. A.; Odriozola, J. A. C. CO_2 reforming of methane over Ni-Ru supported catalysts: On the nature of active sites by operando DRIFTS study. *J. CO2 Util.* **2018**, *24*, 509−515.

(59) Yokomizo, G. H.; Louis, C.; Bell, A. T. An infrared study of CO adsorption on reduced and oxidized $RuSiO_2$. *J. Catal.* **1989**, *120*, 1−14.

(60) Cimino, S.; Russo, R.; Lisi, L. Insights into the cyclic CO_2 capture and catalytic methanation over highly performing Li-Ru/Al_2O_3 dual function materials. *Chem. Eng. J.* **2022**, *428*, 131275−131288.

(61) García-Melchor, M.; López, N. Homolytic Products from Heterolytic Paths in H_2 Dissociation on Metal Oxides: The Example of CeO_2. *J. Phys. Chem. C* **2014**, *118*, 10921−10926.

(62) Hadjiivanov, K. Identification and Characterization of Surface Hydroxyl Groups by Infrared Spectroscopy. In *Advances in Catalysis*; Jentoft, F. C., Ed.; Academic Press: Cambridge, 2014; Chapter 2, Vol. 57, pp 99−318.

(63) Garbarino, G.; Bellotti, D.; Finocchio, E.; Magistri, L.; Busca, G. Methanation of Carbon Dioxide on Ru/Al_2O_3: Catalytic Activity and Infrared Study. *Catal. Today* **2016**, *277*, 21−28.

(64) Upham, D. C.; Derk, A. R.; Sharma, S.; Metiu, H.; McFarland, E. W. CO_2 Methanation by Ru-Doped Ceria: The Role of the Oxidation State of the Surface. *Catal. Sci. Technol.* **2015**, *5*, 1783−1791.

(65) Deshpande, S.; Patil, S.; Kuchibhatla, S. V. N. T.; Seal, S. Size Dependency Variation in Lattice Parameter and Valency States in Nanocrystalline Cerium Oxide. *Appl. Phys. Lett.* **2005**, *87*, 133113−133117.

(66) Chiorescu, I.; Arce-Ramos, J.; Wen-Qing, L.; Genest, A.; Rösch, N. CO_2 reduction by H_2 to CHO on Ru(0001): DFT evaluation of three pathways. *Surf. Sci.* **2019**, *681*, 54−58.

(67) Knut, R.; Karis, O. Spectroscopic Investigations of Electronic Structure. In *Science and Technology of Atomic, Molecular, Condensed Matter & Biological Systems*; Das, T. P.; Sanyal, B.; Eriksson, O., Eds.; Elsevier: Amsterdam, 2012; Chapter 3, Vol. 2, pp 45−70.

(68) Ganduglia-Pirovano, M. V.; Da Silva, J. L. F.; Sauer, J. Density-Functional Calculations of the Structure of Near-Surface Oxygen Vacancies and Electron Localization on CeO_2(111). *Phys. Rev. Lett.* **2009**, *102*, 26101−26105.

(69) Farra, R.; García-Melchor, M.; Eichelbaum, M.; Hashagen, M.; Frandsen, W.; Allan, J.; Girgsdies, F.; Szentmiklósi, L.; López, N.; Teschner, D. Promoted Ceria: A Structural, Catalytic, and Computational Study. *ACS Catal.* **2013**, *3*, 2256−2268.

(70) Skafte, T. L.; Guan, Z.; Machala, M. L.; Gopal, C. B.; Monti, M.; Martinez, L.; Stamate, E.; Sanna, S.; Garrido-Torres, J. A.; Crumlin, E. J.; et al. Selective high-temperature CO_2 electrolysis enabled by oxidized carbon intermediates. *Nat. Energy* **2019**, *4*, 846−855.